Buckling of axially compressed CFRP cylinders with and without additional lateral load

Experimental and numerical investigation

Khakimova, Regina; Castro, Saullo G.P.; Wilckens, Dirk; Rohwer, Klaus; Degenhardt, Richard

Important note
To cite this publication, please use the final published version (if applicable).
Please check the document version above.
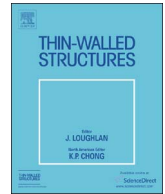
Full length article

Buckling of axially compressed CFRP cylinders with and without additional lateral load: Experimental and numerical investigation

Regina Khakimova[a,b,*,1], Saullo G.P. Castro[c], Dirk Wilckens[b], Klaus Rohwer[b], Richard Degenhardt[b,d]

[a] INVENT GmbH, Christian-PommerStrasse 34, 38112 Braunschweig, Germany
[b] DLR, Institute of Composite Structures and Adaptive Systems, Lilienthalplatz 7, 38108 Braunschweig, Germany
[c] EMBRAER, Brazilian Aerospace Company, 12227-901 São José dos Campos, SP, Brazil
[d] PFH, Private University of Applied Sciences Göttingen, Composite Engineering Campus Stade, Germany

A B S T R A C T

Thin-walled structures are widely used in aerospace, offshore, civil, marine and other engineering industries. Buckling of such thin-walled imperfection sensitive structures is a very important phenomenon to be considered during their design phase. Existing design guidelines, being the most known the NASA SP-8007 for cylinders dated from the late 1960's are currently used in the aerospace industry and employ conservative lower-bound knock-down factors. These empirically based lower-bound methods do not include important mechanical properties of laminated composite materials, such as the stacking sequence. New design approaches that allow taking full advantage of composite materials are therefore required.

This study deals with buckling experiments of axially compressed, unstiffened carbon fiber–reinforced polymer (CFRP) cylinders with and without an additional lateral load. Two geometrically identical cylinders with the same layup were designed, manufactured and tested. Before testing, the thickness of the cylinders was measured with ultrasonic inspection and the geometry was measured utilizing a 3D scanning system based on photogrammetry. During testing, a digital image correlation system was employed to monitor deformations, strain gage readings and load-shortening data was taken. Modelling of shape mid-surface and thickness imperfections as well as fiber volume fraction correction are included into the Finite Element Analysis (FEA) of the test structures, and the experimental results are compared against FEA results.

1. Introduction

Thin-walled structures like cylindrical shells are used as primary structural parts in space launch vehicles. These structures carry heavy loads and are therefore subjected to axial compression which makes buckling one of the limiting design constraint.

Buckling of thin-walled structures has been studied by many researchers both, theoretically and experimentally since the beginning of the last century. It was noticed that the experimental buckling load is much lower than the theoretical buckling load. Koiter showed in 1945 [1] that the difference between the theoretical buckling load and the experimental load of thin-walled structures is predominantly due to the influence of geometric imperfections. Within this paper, geometric imperfections are defined as deviations of the real mid-surface from its nominal shape. A considerable amount of effort was put into developing analytical, semi-analytical, empirical and numerical strategies that take imperfections into account. Currently industry uses the NASA SP-8007 guideline [2] to design thin-walled cylinders. The principle of the design procedure is to employ a Knock-Down Factor (KDF) that is multiplied to the theoretical buckling load in order to calculate the design buckling load. The guideline presents a formula for the KDF, obtained from a lower bound curve of experimental results. One problem is that the guideline does not consider all material characteristics of composite structures appropriately. Secondly, the test data which serves as the base for the empirical KDFs is not well-documented and its quality is hard to assess. As mentioned in [3], some of the scatter in the test data can be due to the uneven load introduction or non-accurate representation of the boundary conditions. Another issue is that modern manufacturing and test techniques got more advanced than the ones from the last century. Finally, it was observed that the NASA SP-8007 KDF delivers buckling loads much lower than the ones detected during experiments [4–6]. Many authors concluded that the NASA design

---

approach is too conservative for modern composite and metallic thin-walled structures (for example Arbocz and Starnes [7], Hilburger [4,8], Degenhardt et al. [9,10]). Recently there was a lot of effort put into developing new design guidelines for thin-walled shells. As an alternative to NASA SP-8007, a deterministic design approach for cylinders, the so called Single Perturbation Load Approach, was proposed by Hühne [5]. It was suggested that stimulating the initial imperfection by applying the lateral load one can simulate a realistic geometric imperfection and use the imperfect model in the design phase. The background and published work on the SPLA is next reviewed.

1.1. State of the art

In 1970, during the buckling experiments conducted by Esslinger [11] using high-speed cameras, it was observed that the buckling process always starts with a single buckle. The pattern then develops around the circumference until finally a diamond shaped postbuckling pattern is reached. These observations led to the conclusion that an imperfection in the form of a single buckle could be considered as suitable to disturb the structure towards buckling. Deml and Wunderlich [12] also came to this conclusion using a modified finite element procedure in which the nodal coordinates were included in the set of unknown degrees of freedom, allowing the solver to find not only the nodal displacements but also the worst nodal positions that, within a given mobility tolerance (i.e. the maximum imperfection amplitude), would minimize the buckling load. Hühne et al. [5] proposed to stimulate a single buckle by applying a lateral point load, in order to investigate the imperfection sensitivity and to achieve a realistic geometric imperfection representation that could be used even at the early design phases, where the real imperfection pattern of the structure is still unknown. Their studies resulted in a proposal for a new deterministic design approach for thin-walled cylinders that takes into account geometric imperfections, called the Single Perturbation Load Approach (SPLA), which is less conservative than the NASA SP-8007 but still a lower bound for the cylinder design treated [5]. The idealization of a typical SPLA knock-down curve is shown on the right in Fig. 1 which depicts the buckling load (N) versus the perturbation load (PL). As one increases the value of the perturbation load, the buckling load reduces until it approaches a threshold where it remains nearly constant. This threshold of PL is called P1 (see point 1 in Fig. 1) and the corresponding buckling load is called N1, which is assumed to be the design load when using the SPLA.

In previous studies the SPLA was investigated with cylindrical structures, for example [13,14], as well as with conical structures [15,16]. Arbelo et al. [13] compared the NASA SP-8007 and the SPLA design methodologies and validated it with the experimental results of buckling tests of 48 composite cylinders with different layup found in the literature. They discovered that the SPLA delivers knock-down

factors which are conservative with respect to the experiments in most of the cases and are at the same time less conservative than the NASA KDFs.

Castro et al. [14] have compared the SPLA with other deterministic sizing methods. These studies have shown that axisymmetric imperfections or the imperfections coming from linear buckling modes may result in a much smaller knock-down factor using the same imperfection amplitude as the dimple produced by a single perturbation load. However, some of these methods may be unrealistic in the sense that the imperfection pattern produces results that are not observed in real test conditions (Haynie and Hilburger [17], Hilburger [4]), e.g. a significant reduction of the axial stiffness prior to buckling. Moreover, the aim in the design process is not using the worst imperfection but the imperfection close to the representative and realistic one. As it was shown, the SPLA design load appeared to be more conservative than the buckling load of models with the geometric imperfections [18]. Besides, the method does not reduce the axial stiffness of the structure. To sum up, the SPLA is a deterministic lower bound approach that has shown to be a reliable method to account for geometric imperfections [19] and less conservative than the current design guideline when applied to unstiffened composite cylinders. Load introduction and boundary condition imperfections that could take place are not aimed to be covered by the SPLA [20,21].

In the scope of this work and within the frame of this methodology the KDF is obtained using the following formula:

$$KDF = \frac{N_1}{P_{cr}} \tag{1.1}$$

where P_{cr} is calculated in this paper with FEA using a Lanczos eigensolver [22] and corresponds to the first eigenvalue of the linear buckling analysis of the perfect cylinder.

1.2. Goal

The study deals with the buckling experiments of axially compressed, unstiffened CFRP cylinders performed at DLR for validation of high-fidelity numerical models and, additionally, for validation of the SPLA for a particular composite cylinder configuration (geometric parameters and stacking sequence that was not tested before). All tested structures are non-destructively inspected before testing and measured with a photogrammetry system during the tests. Besides, the goal is to verify if the NASA SP-8007 is conservative for the laminated composite cylinders under axial compression of this certain configuration. The KDF predicted by the SPLA is compared with the KDF of the structures with modeled geometric imperfections. Finally, the aim is to contribute to the general empirical data of composite thin-walled cylinders subjected to axial compression for design purposes.
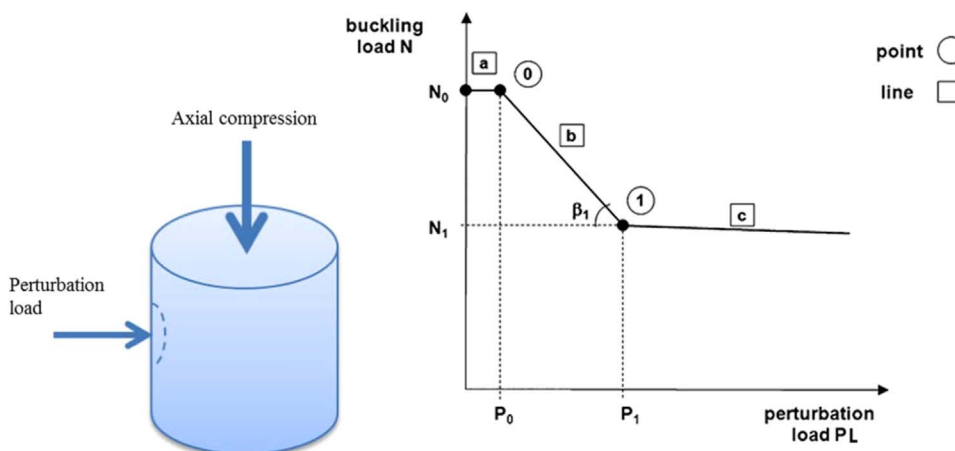
Fig. 1. Left: schematic mechanism of SPLA. Right: idealized curve of buckling load versus perturbation load taken from [5].

Table 1
Characteristics for Z36 and Z37.

Stacking sequence	$[34/-34/0/0/53/-53]$
Radius, R	400 mm
Thickness, t	0.75 mm
Height, H	800 mm
R/t	533
L/R	2
Material properties	$E_{11} = 152.4$ GPa, $E_{22} = 8.8$ GPa, $\nu_{12} = 0.31$, $G_{12} =$ 4.9 GPa, $G_{13} = 4.9$ GPa, $G_{23} = 3.23$ GPa

2. Test structures

The test articles have been designed in such a way that they remain intact after buckling in order to withstand several tests for various configurations of perturbation load. The cylinders were manufactured in-house at the Institute of Composite Structures and Adaptive Systems of DLR by prepreg hand layup on a mandrel and cured in an autoclave. The structures' material is IM7/8552, a unidirectional (UD) prepreg with carbon fibers and epoxy matrix. The material properties were obtained through coupon testing according to the German standards ([23–26]). The material as well as the nominal geometry data and the stacking sequence of the two test structures Z36 and Z37 are given in Table 1. Note that the measured moduli for longitudinal compression (E_{cL}) and transverse tension (E_{tT}) are used for E_{11} and E_{22}, respectively. The shear modulus G_{23} was not experimentally measured and is calculated using the approximation formula taken from Schürmann [27].

The cylinders were potted into the metal rings with a height of 20 mm using an epoxy resin system. That means that the overall height of the structure was 840 mm and the free height of the test article excluding the metal rings was 800 mm. A cylinder with the potting is shown in Fig. 2 (left).

The thickness of the cylinders was measured with ultrasonic inspection and the geometry was measured utilizing the 3D scanning system based on photogrammetry, ATOS. The ultrasonic test is carried out with a broadband transducer in echo-technique, and the results can be displayed as A-, B, C- or D-scan. The D-scan results showing the thickness distribution of for both test structures are given in Fig. 3. A-TOS, an optical 3D digitizing measurement system based on photogrammetry, is utilized to extract the initial geometric imperfections of the shell using a best-fit procedure aimed to eliminate rigid body motion modes from the measurements [28]. The deviation from the ideal geometry of the cylinders generated from the measured points is given

as false color plot (Fig. 4). More detailed description on these non-destructive inspection methods and evaluation of the measurement results are given in [29].

3. Test set-up

3.1. Buckling test setup and instrumentation

The CFRP cylinders were tested under axial compression in the buckling test facility of the Institute of Composite Structures and Adaptive Systems of DLR (Fig. 5 left). The test article is located between an axially supporting top plate and a lower drive plate. The top plate can be moved in vertical direction on three spindle columns to adapt the test device to various test article lengths.

A thin epoxy concrete layer is applied between the end plates of the test specimens and the adjacent parts of the test device. This procedure is done to ensure a uniform load introduction on the test structure during loading. Loads and axial displacements are recorded during the tests. The actual reaction loads are measured by three load cells (100 kN each). The axial displacement is extracted by three displacement transducers, fixed between the load distributer and the axial drive and placed around the test specimen at 90°, 180° and 270°. The structures are additionally instrumented with several back-to-back strain gages. A multi-channel data acquisition system is used to record the readings of the load cells, strain gages and the displacement transducers.

The test setup of the test cylinder with an applied lateral load is shown in Fig. 5 (right). The lateral load is applied normally on the surface of the shell inducing a single buckle. The lateral loading device is fixed using magnets. With different weights, it is possible to vary the magnitude of the lateral loading. The position of the point load can be varied in the circumferential and meridional direction. First, constant lateral load is applied on the structure and then the displacement-controlled axial compression is applied and progressively increased.

Back-to-back strain gages are applied to measure the strains in the axial direction and to detect bending effects in the shell prior buckling, as shown in Fig. 6. In case of Z36, 24 UD strain gages are placed at 0°, 60°, 120°, 180°, 240° and 300° as well as 6 rosettes at 0°, 120° and 240°. The rosette strain gages are placed in the middle of the shell's height, whereas the lower and the upper rows of the strain gages are positioned 100 mm below and 100 mm higher from the upper and lower shell's edges, respectively (cf. Fig. 6(a)). A total number of 18 UD strain gages
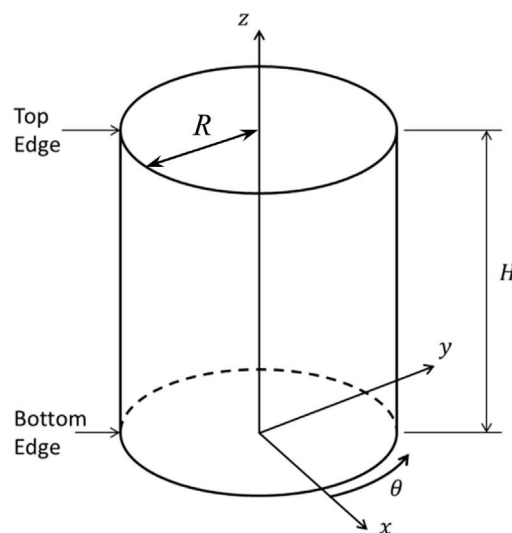
a) real structure with potting   b) structure's geometry

Fig. 2. Test structure. a) real structure with potting. b) structure's geometry.
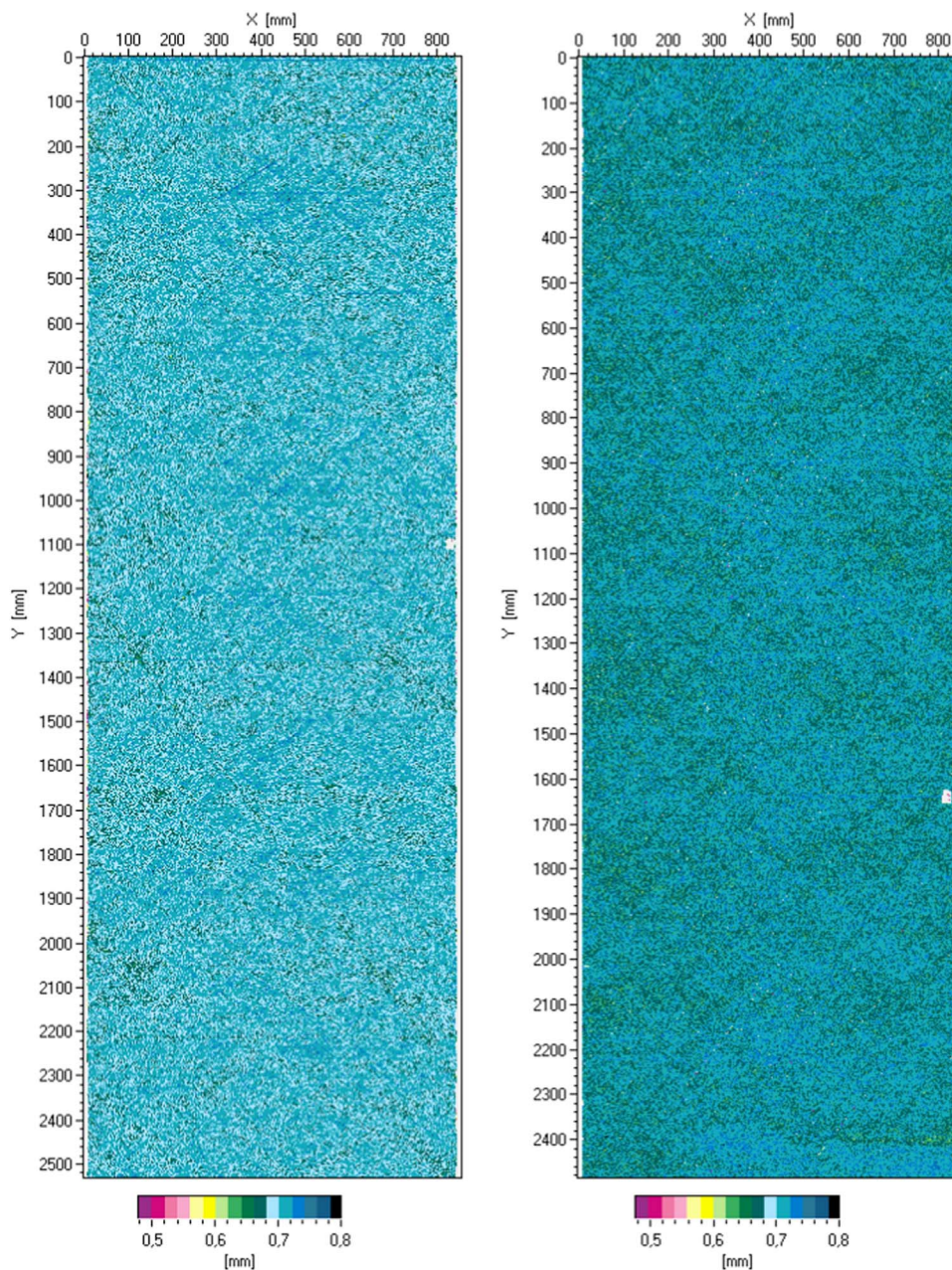
Fig. 3. D scans of Z36 (left) and Z37 (right).

in case of Z37 are positioned circumferentially at 60°, 180° and 300° as shown in Fig. 6(b).

A digital image correlation system, ARAMIS, is used for measurement of the deformation behavior of the test specimen. The ARAMIS (12 M) system [30] records the deformation field (in-plane and out of plane) of a test article under loading using a pair of cameras. Before testing, the test article must be speckled in a black and white pattern. One ARAMIS measurement system can cover about 30% of the entire cylinder's surface. The measurement field is chosen to be in the front of the structure, covering the area between θ = 300° and 30°.

3.2. Test description

A number of buckling experiments was carried out with both test cylinders. That was possible because the cylinders buckle elastically and stay intact after many tests (as intended in the specimen design) since the load is applied displacement controlled. During the buckling tests the magnitude of the perturbation load are varied in order to get a

typical perturbation load curve (see Fig. 1 (right)). In case of Z36 the PL is applied at three different circumferential positions: θ = 30°, 150° and 210°, whereas in case of Z37 the PL was applied only at θ = 30°. The perturbation load values are varied from 0 N to 20 N.

4. Test results

The test results are given in terms of load-shortening curves, strains, perturbation load curves and selected out-of-plane deformation patterns (ARAMIS). The tests have been conducted several times with each structure according to the test plan described above (Section 3.2).

4.1. Buckling load and stiffness

The buckling load values of Z36 and Z37 are rounded to one digit after comma and are shown in Table 2 in the chronological order of the tests. As it can be seen the buckling load value of the same cylinder fluctuates slightly. However, this is not due to a degradation of the
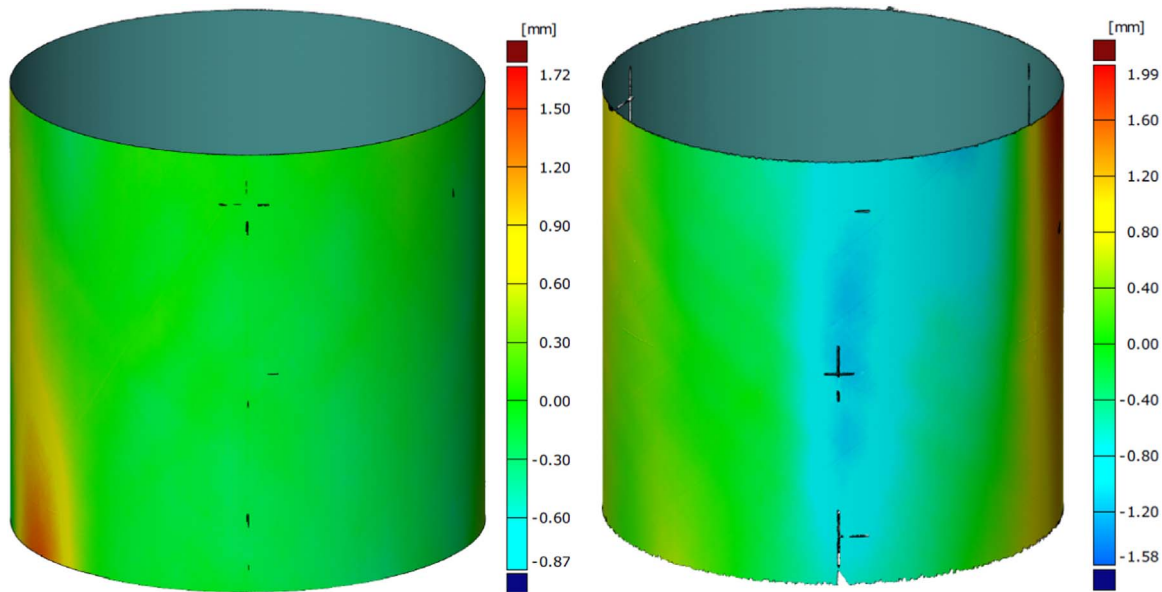
Fig. 4. Front view of ATOS measurement results for Z36 (left) and Z37 (right).
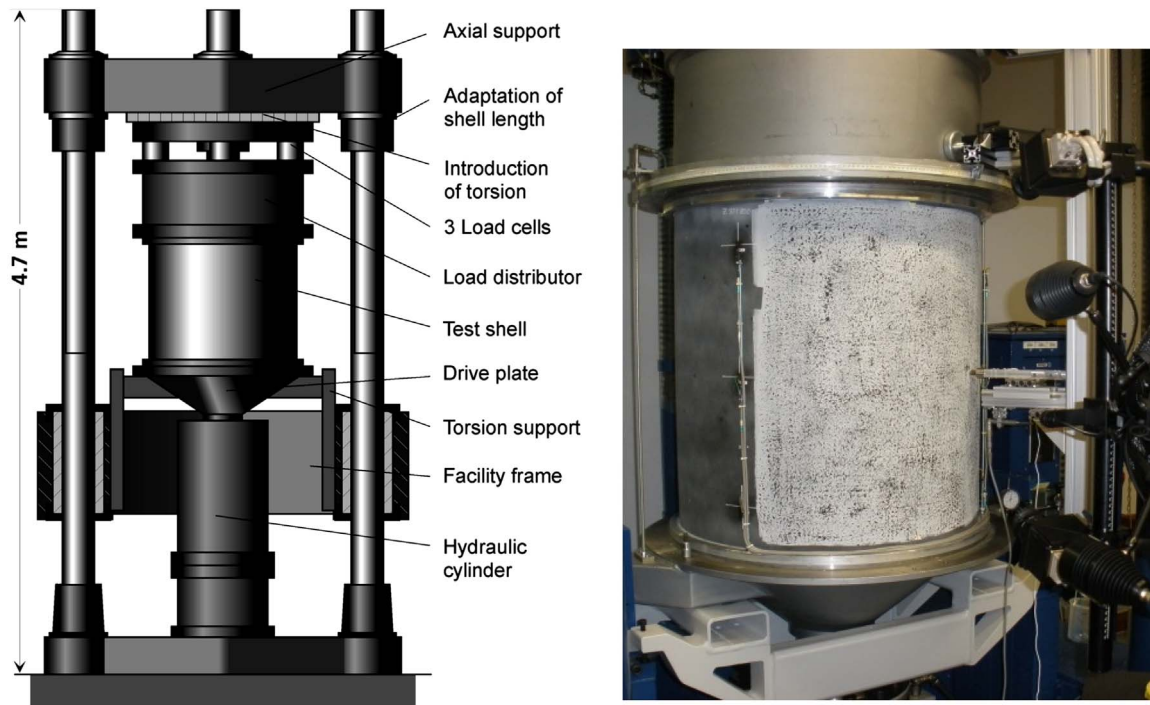
Fig. 5. Buckling test facility (left), test setup with the applied lateral load (right).

structure, but due to the scatter of the whole measurement and data acquisition chain (including the load cells). The important observation is that the stiffness of the structures remains the same during repeated testing.

The measurements of the test specimens' deformation using the DIC system (ARAMIS) were performed on some buckling tests selectively. The measured displacement field of Z36 and Z37 at several points along the load-shortening curve is shown in Fig. 7, where automatic scaling for each frame is utilized. This means that different scaling is used between the frames in order to visualize the small displacement amplitudes in the prebuckling pattern as well as the larger ones in the postbuckling pattern. In the prebuckling regime, the scaling of the images is comparable, whereas in the postbuckling regime it isn't due to the higher shortening. The displacement pattern of the test structures in

the prebuckling regime differs from each other due to the different imperfection shape. The postbuckling pattern is well comparable between the two test articles considered and is equally developed around the structure. Both cylinders buckle with 2 rows of dimples: 12 in each row in case of Z36 and 13 buckles in each row in case of Z37.

Regarding the axial stiffness, two observations are made for Z37. First, the stiffness, measured between a shortening of 0.2 mm and 0.3 mm is found to be about 14% lower than the one of Z36 measured between 0.2 mm and 0.3 mm. Secondly, the axial stiffness of Z37 is in contrast to Z36 slightly increasing at the beginning of the loading until almost 0.2 mm before the final stiffness is reached. For these two effects, different reasons and explanations are supposed. For the increasing stiffness at the beginning of the load shortening curve of Z37, it is assumed that geometric imperfections in the load introduction, i.e. in
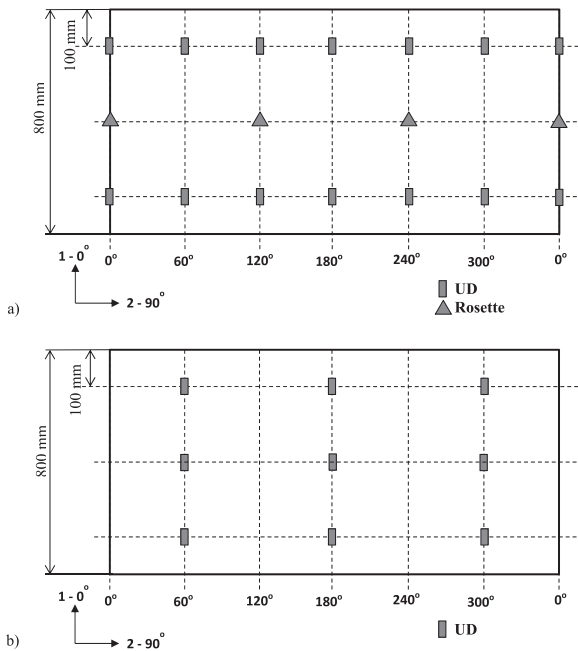
Fig. 6. Strain gage plan a) Z36 b) Z37.

Table 2
Buckling load values for Z36 and Z37.

Test sequence	Z36	Z37
1	64.0 kN	57.5 kN
2	63.6 kN	56.8 kN
3	63.4 kN	57.5 kN
4	63.1 kN	59.2 kN
5	63.0 kN	59.3 kN
6	62.5 kN	59.3 kN
Mean value	63.3 kN	58.3 kN

the equalizing layer between the load distributor of the buckling test facility and the upper end plate of the cylinder, lead to slight loading asymmetries. This results in minor non-uniform loading so that parts of the specimen are loaded first, while other parts are still unloaded. This assumption is also corroborated by the strain gauge readings for this cylinder and can also be seen in the individual results of the displacement transducers described in the next paragraph. The interface is prepared for each test article individually and therefore slight inhomogeneities might have been introduced for the test of Z37. However, the difference in the final axial stiffness once the load is

transferred around the circumference can no longer be attributed to load asymmetry. Therefore, other reasons like fiber angle deviation and fiber volumetric fraction may be playing an important role explaining this difference between these two nominal identical test specimens.

4.2. Displacement transducers

The individual readings of the displacement transducers are analyzed to monitor possible asymmetry in the load introduction between the load distributer and the axial drive plate (Fig. 5). In Fig. 8 the result of this assessment is given for Z36 and Z37 for tests without perturbation load. The three curves are plotted against the mean value of their summation, where constant offsets resulting from installation of the displacement transducers are removed. The load shortening curve is also given in the plot to correlate the initiation of buckling with the axial displacement readings. In the case of Z36, cf. Fig. 8 (left), the lines of the sensors remain practically coincident until the point of the buckling, indicating that upper and lower plates remain parallel with respect to each other. The deviation is found to be below the measurement accuracy of the displacement transducers. In the postbuckling regime there are some fluctuations, indicating that the plates tilt slightly due to the stiffness redistribution in the cylinder. It can be assumed that no relevant load asymmetry takes place in the load introduction between the load distributer and the axial drive plate during the Z36 buckling tests.

However, in the case of Z37, the three curves slightly diverge from each other within increasing axial shortening as a result of the assumed imperfection in the load introduction interface (see Fig. 8 (right)). The maximum difference of the displacement transducer readings at the buckling point is about 0.03 mm, which indicates that the load is unevenly applied during the buckling test of Z37 as described above.

As discussed in the previous section and shown in [31], load asymmetry affects the buckling load and, additionally, causes an initial axial stiffness transition. But once the load is transferred around the circumference the deviation in the final axial stiffness is not caused by load asymmetry. The difference of the stiffness of Z37 in comparison to Z36 can be attributed to fiber angle deviation, fiber volumetric fraction or any other errors and deviations caused by manufacturing.

4.3. Strains

The values of the membrane strain (ϵ_m) and the bending strain (ϵ_b) can be calculated according to the equations below, based on the strains measured by the gages on the inside surface (ϵ_{inside}) and the outside surface ($\epsilon_{outside}$). In this paper κ is denominated as the bending fraction which is defined as the ratio of membrane to bending strain, as given below:
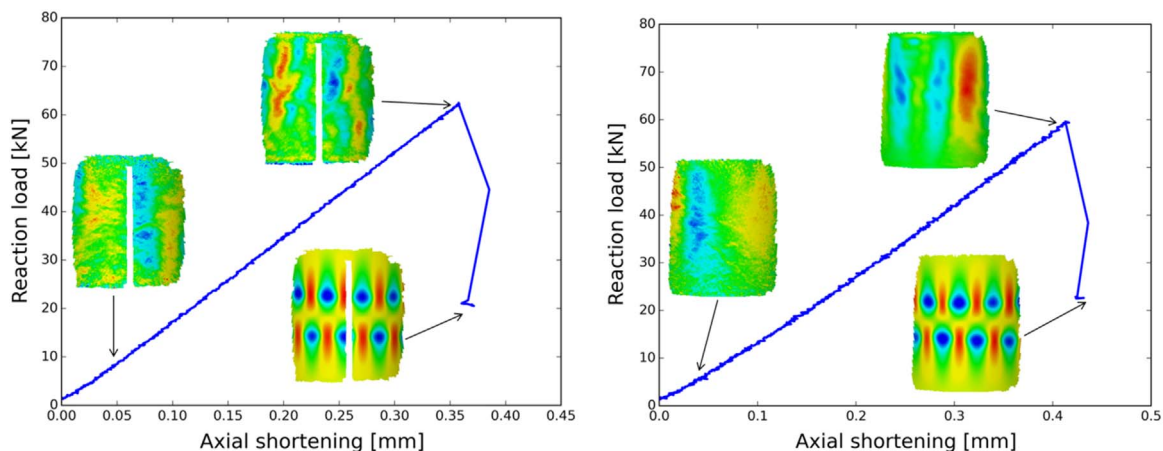
Fig. 7. Load shortening curves for Z36 (left) and Z37 (right).
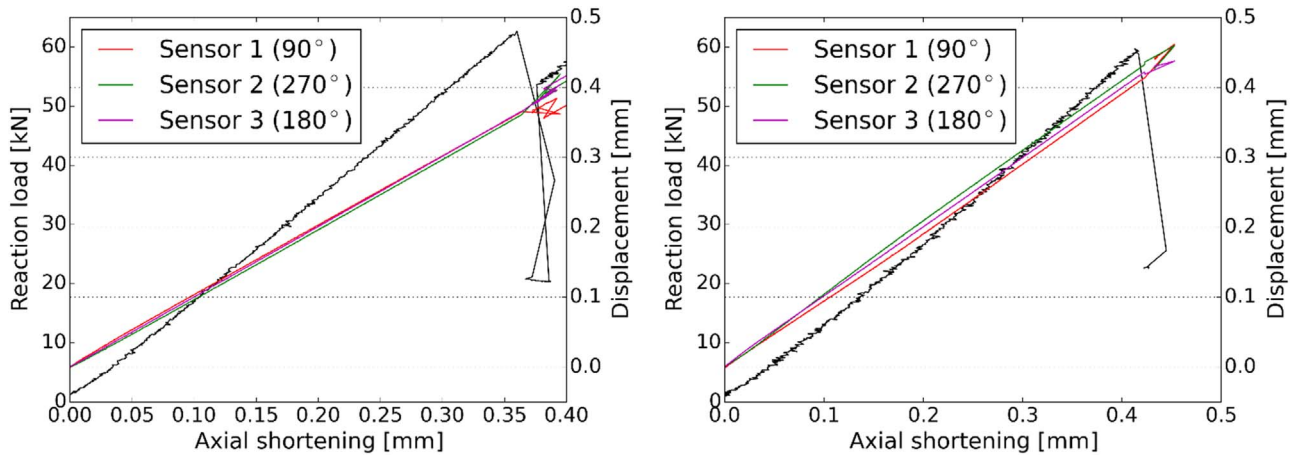
Fig. 8. Displacement transducer readings together with the load shortening curve for Z36 (left) and Z37 (right).

$$\epsilon_m = \frac{1}{2}(\epsilon_{inside} + \epsilon_{outside}) \qquad (4\text{-}1)$$

$$\epsilon_b = \frac{1}{2}(\epsilon_{inside} - \epsilon_{outside}) \qquad (4\text{-}2)$$

$$\kappa = \frac{\epsilon_b}{\epsilon_m} \cdot 100\% \qquad (4\text{-}3)$$

Fig. 9 includes two rows of plots where the top row shows the membrane strains as a function of the circumferential position, for respectively the upper, middle and lower strain gages (see strain gage plan in Fig. 6). The strains are plotted at four load levels: 25%, 50%, 75% and 100% of the buckling load for each cylinder. The strain is measured in three positions (marked 'x'), through these three points a sine wave (dashed line) was chosen for fitting. The extrema of this sine wave are indicated with a diamond symbol ◊. The bottom row of plots shows the bending fraction for respectively the upper, middle and lower set of strain gages. Note that some amount of filtering was applied to create this curve, in order to remove the (otherwise excessive) noise. A linear forward-backward Python function *filtfilt* is used to filter the plotted data.

The values of the membrane strains are not perfectly uniform in the circumference direction during loading for Z36 (Fig. 9); the absolute value of the membrane strain is consistently lower around 120° for the upper, middle and lower strain gages. This suggests that there is some sort of gap or other imperfection around this circumferential location, causing an uneven membrane force distribution in the cylinder. The most significant bending occurs at 120° and 0° in the middle strain gage. While the displacement transducers readings of the tests with Z36 showed relatively even loading distribution, possible imperfections in the interface of the potting and the shell with the plate may take place and cause an imperfect load distribution in the cylinders.

In case of Z37 the absolute value of the strain is lower around 300° than in the other positions around the circumference as it can be seen in Fig. 10. The most uneven membrane strain values are in the upper strain gage. The bending plots show that there is significant bending taking place at 180° in the middle and lower strain gage. The bending might occur not only due to the imperfect interfaces and boundary conditions, but also due to the slight load asymmetry as shown in Fig. 8(right).
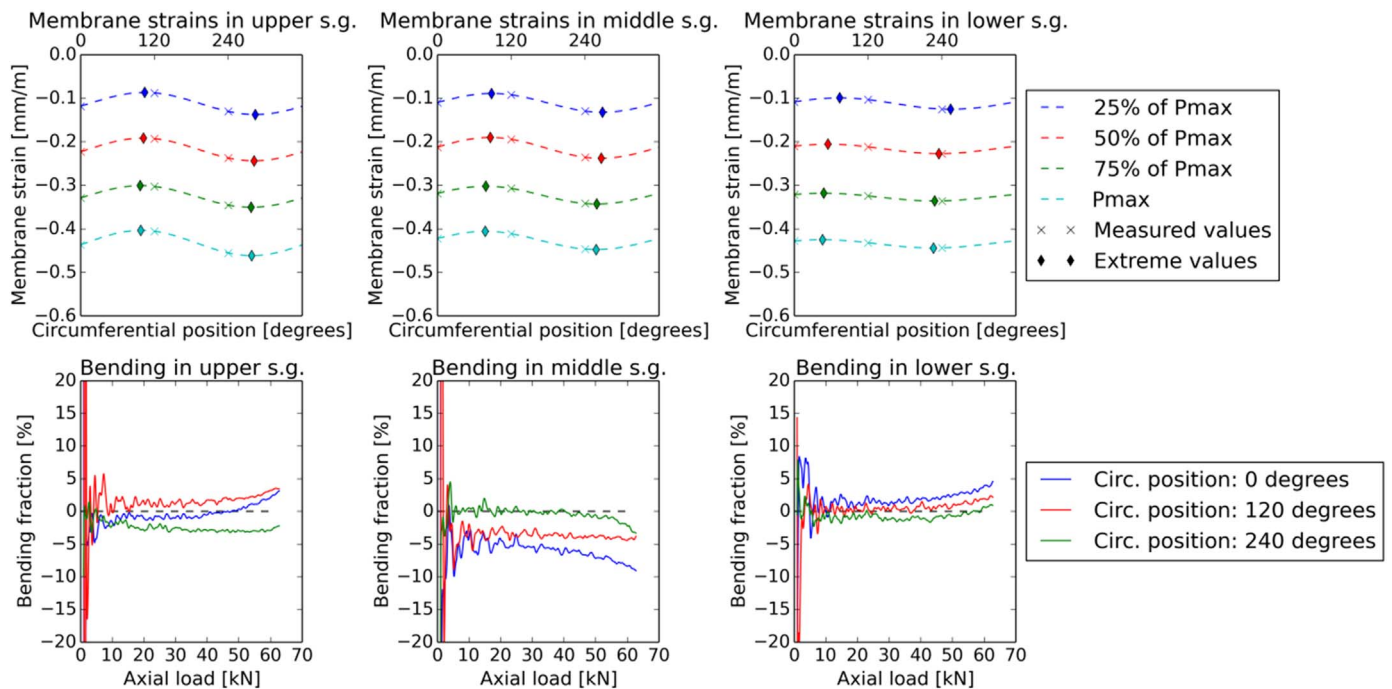
Fig. 9. Membrane strains and bending fractions for Z36, without PL.
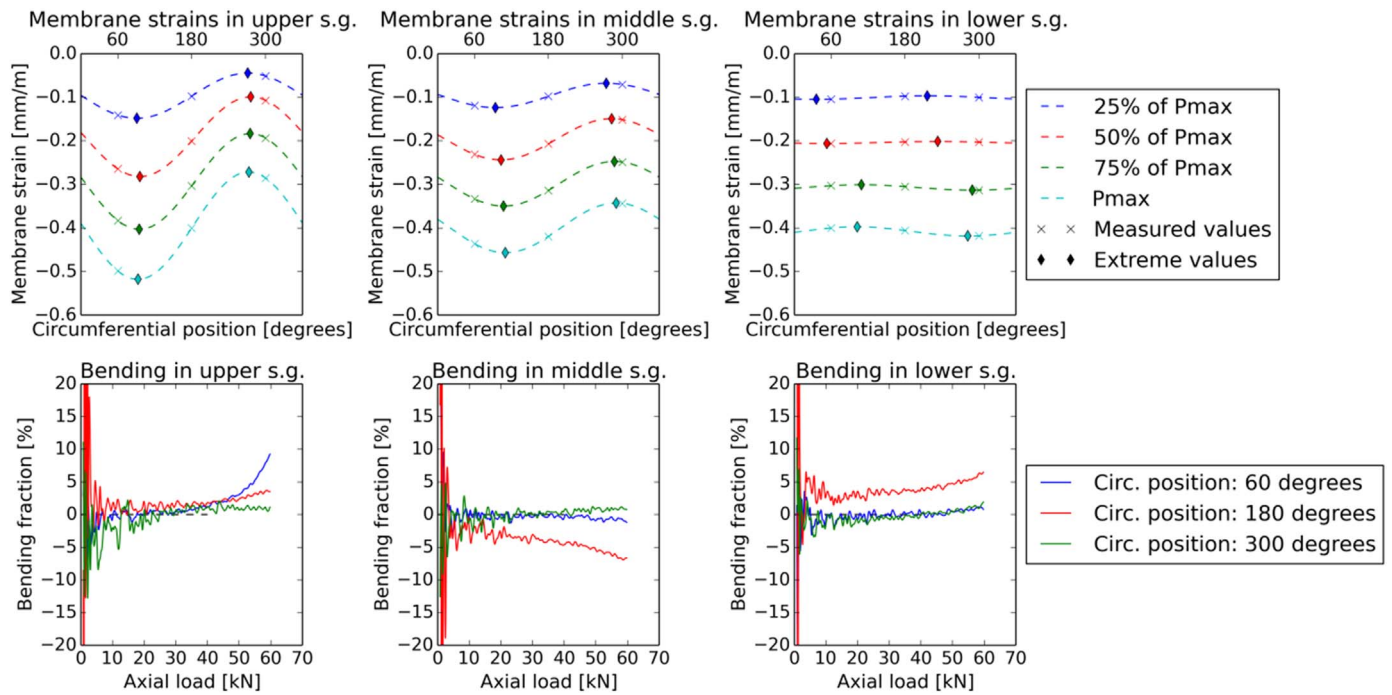
Fig. 10. Membrane strains and bending fractions for Z37, without PL.

4.4. Test results with additional lateral load

The load-shortening curves of Z36 at θ = 30° along with the corresponding perturbation load curve are depicted exemplarily in Fig. 11, showing the effect of the lateral load on the buckling load. These experimental results reflect the SPLA phenomenon: after a certain PL value, in this case 9 N, the reaction buckling load remains nearly the same for tests with the different application perturbation load position and different values of the perturbation load. That means that in this case P1 is 9 N and the corresponding buckling load N1 is around 52 kN.

5. FEA modelling

5.1. Parameters

For the Finite Element Analysis (FEA) ABAQUS Standard 6.14 (Implicit) combined with the plugin developed by Castro et al. [28] within the scope of the DESICOS project was employed. The Newton-

Raphson iterative procedure with artificial damping stabilization was used as the non-linear solver. The parameters for FEA are shown in Table 3.

The numerical model of the cylinder is meshed using shell elements of type "S8R". This is a thin shell element with 8 nodes, six degrees of freedom per node and reduced integration. The number of elements in the circumferential direction is 160, based on the results of a convergence study. The element size in the other direction is chosen automatically so that the element length aspect ratio is kept close to 1. The perturbation load PL is applied perpendicularly to the cylinder surface in the middle of the cylinder's height and at an angular coordinate θ = 30°, 150° and 210.

5.2. Perfect model

Fig. 12 (left) shows the meshed FE model whereas Fig. 12 (right) shows the first linear buckling mode of the perfect model obtained in this paper using Lanczos eigensolver [22]. The linear buckling load,

a) Load-shortening curves

b) Perturbation load curve
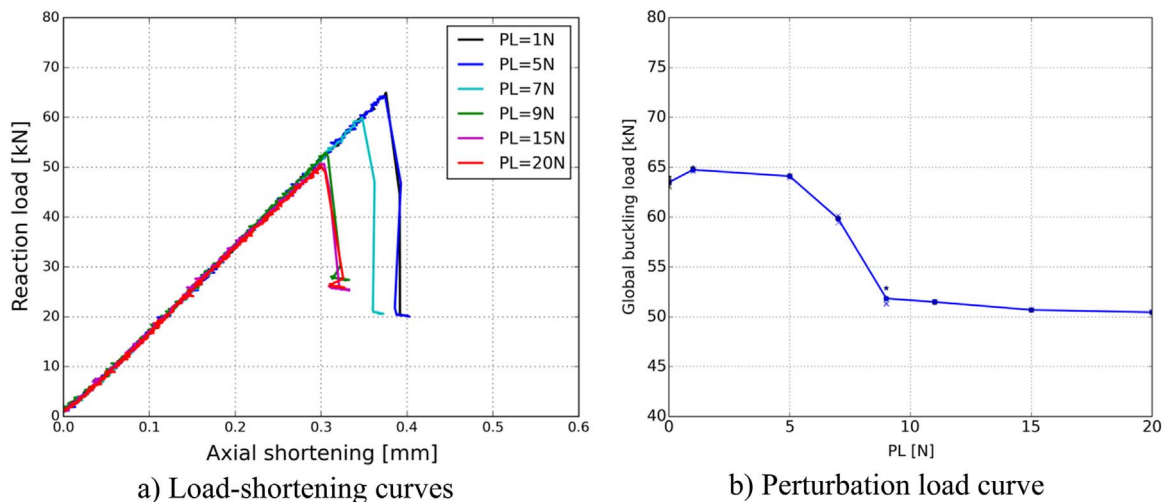
Fig. 11. SPLA diagram of Z36 at θ = 30°, a) Load-shortening curves, b) Perturbation load curve.

Table 3
FEA parameters.

Element type	S8R
Number of elements around circumference	160
Boundary conditions	Clamped edges
Damping factor	1×10^{-7}
Initial increment	0.001
Maximum increment	0.001
Minimum increment	1×10^{-6}
Maximum number of increments	10000

which corresponds to the first eigenvalue of the linear buckling analysis of the perfect cylinder, is the reference load for determining the KDF and equals to 89.6 kN.

Fig. 13 shows the perturbation load curve of the perfect structure, where it can be seen that the resulting design load N1 equals 65.2 kN.

5.3. Model with imperfections

The real built cylinder deviates from the nominal perfect model. These deviations can be described by the mid-surface imperfection (MSI), thickness imperfection (TI), fiber volume fraction (FVF) correction and are considered for the finite element modelling of the imperfect cylinders in this work. Detailed description on the non-destructive inspection procedure and modelling of MSI, TI and FVF is given in [29].

The finite element models of the imperfect cylinders Z36 and Z37 are shown in Fig. 14, where the deviations with respect to the nominal geometry have been scaled by a factor of 100 to make them clearly visible. Although both cylinders were manufactured on the same mandrel, their real shapes differ from each other. The different imperfection patterns might be caused by manufacturing or when demolding the cylinders from the mandrel, whereas it is also possible that some of the dimples in the structures might have been induced during the potting process. After applying the imperfections to the mesh in ABAQUS, the resulting offsets can be plotted. This results in contour plots shown in Fig. 15.

The influence of individual imperfections on the buckling load and the stiffness of Z36 are first investigated individually. Additionally, a combination of all considered imperfections is also investigated. The load-displacement curves of the simulations without perturbation load are used to determine the stiffness. Fig. 16 shows the load-displacement curves of the prefect cylinder, the model with all imperfections (MSI, TI

Fig. 13. Perturbation load curve of the ideal cylinder to determine the design load N1.

+ FVF), all imperfections with the resin rings (as shown in Fig. 2 left) along with the models that contain these imperfections separately. Moreover, the test load shortening curve of Z36 is also given for comparison. It can be seen that the individual imperfections affect the buckling load more than the stiffness. The modeled real measured imperfections in the form of MSI reduce the buckling load more significantly than the TI and FVF. The buckling load obtained by the FE model which includes all measured imperfection still deviates by about 12.7% from the experimental buckling load. This deviation is probably caused by the load introduction imperfections which can be seen from the membrane strains in Figs. 7 and 8. The corresponding FE model that includes all imperfections correlates nevertheless well with the test results and is therefore used for validation purposes of the high-fidelity model and the design method. The differences still observed between the FE model and the test results can be attributed to load asymmetries, which are not included in these numerical simulations.

6. Comparison

In Section 6.1 the validation of the FEA results by experiments is presented and discussed by means of the buckling loads in the form of the perturbation load curves. Section 6.2 compares and discusses the KDF values obtained by the tests, NASA SP-8007 and SPLA.
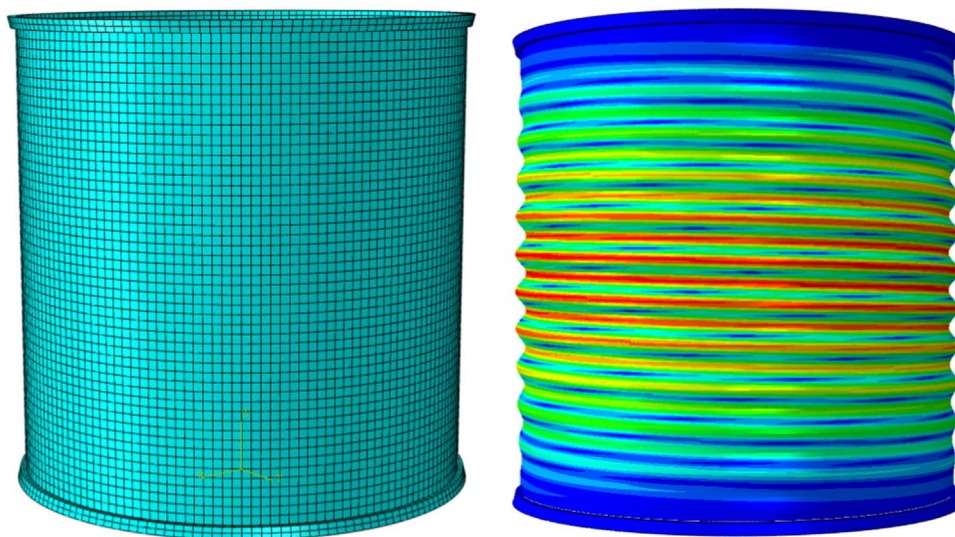
Fig. 12. Left: Meshed cylinder with resin rings. Right: First linear buckling mode of the perfect cylinder.
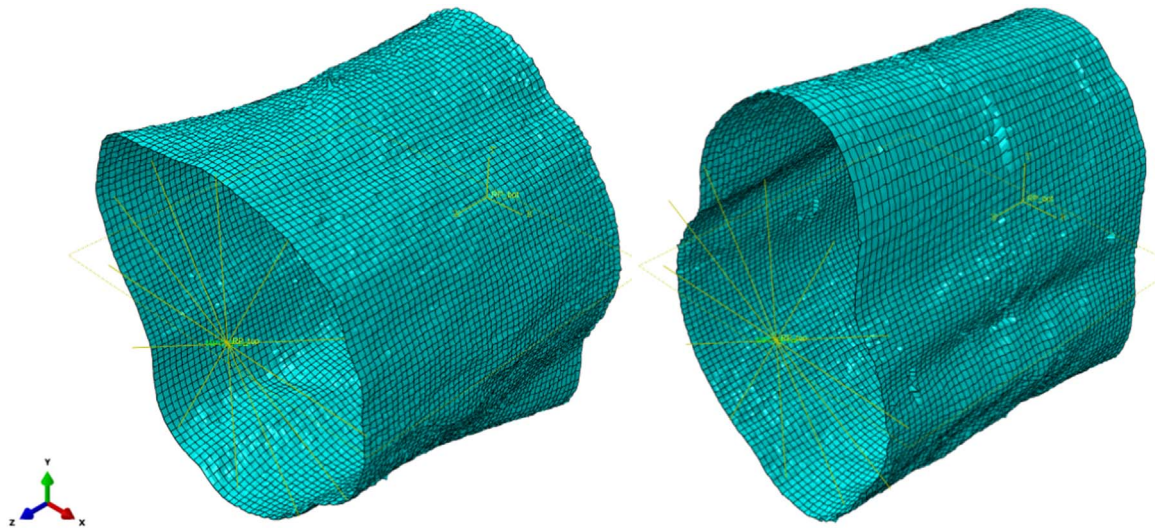
Fig. 14. Mesh with the applied imperfections of Z36 (left) and Z37 (right) scaled 100x.

6.1. Perturbation load curves

As described in Section 3.2, the lateral load was applied at three circumferential positions, namely 30˚, 150˚ and 210 in case of Z36 and 30˚ in case of Z37. The perturbation load values vary from 0 to 20 N. Fig. 17 shows the perturbation load curves of Z36 and Z37 with the lateral load applied at z/H = 0.5 where both, the experimental and simulation results are depicted. The simulated FEA model includes the mid-surface imperfection (MSI), thickness imperfection (TI) and fiber volume fraction (FVF) correction. Additionally, the perturbation load curve of the perfect structure is shown in blue for comparison. There were 5 experiments performed without applying the PL, whereas three experiments for each PL value were carried out. The simulated curve depicted as a solid line with the individual simulations indicated with solid dots. The experimental results are denoted using the markers ★ and •. The former symbol is then used for the first of the three tests and the latter for the subsequent experiments. A dashed line is drawn through the average values of the experimental results. The red lines refer to the results with the lateral load applied at 30˚, the green curves represent the buckling load values with the lateral load applied at 150˚ whereas the purple ones – at 210˚.

The values of N1 and P1 around the circumference differ in case of Z36, which is expected because the structures have imperfect
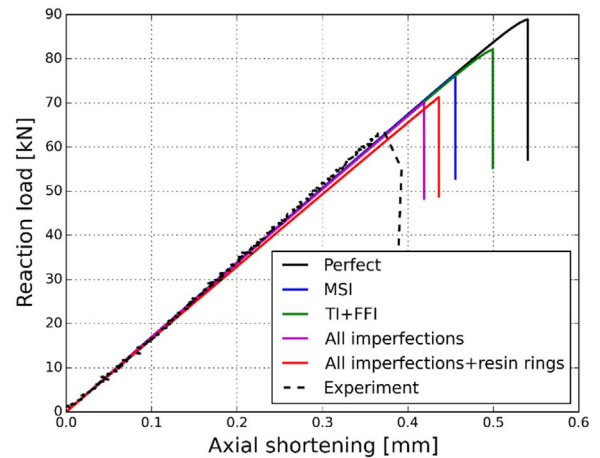
Fig. 16. Load shortening curves of the FE models including individual and all imperfections as well as the test result without perturbation load of Z36.

geometries. The FEA results of the imperfect model correlates very well with the experimental results, apart from the case when the PL is applied at 210˚. The FEA buckling load value of N1 at 210˚ is almost 18% higher than the experimental one. As shown in Fig. 7, bending effects
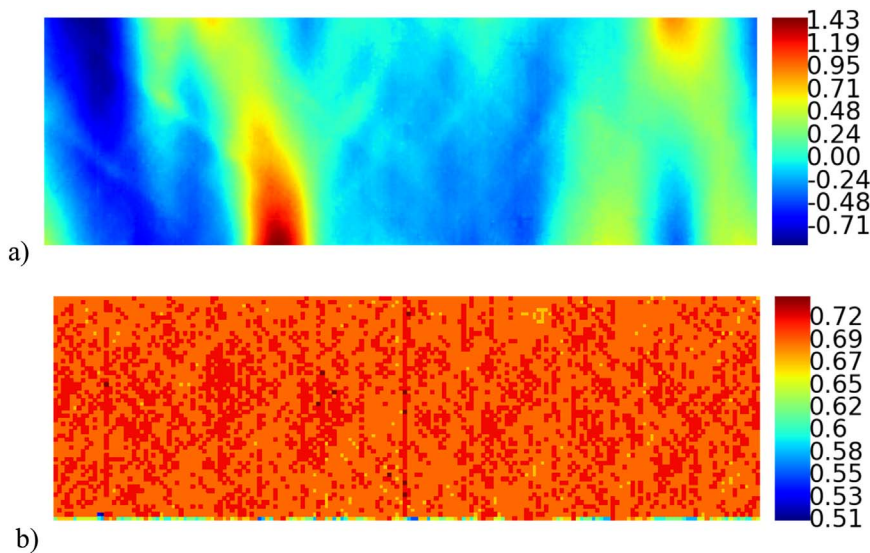
Fig. 15. Imperfection amplitude in mm for Z36, based on data from ATOS scan b)Thickness in mm for Z36, based on data from ultrasonic scan.
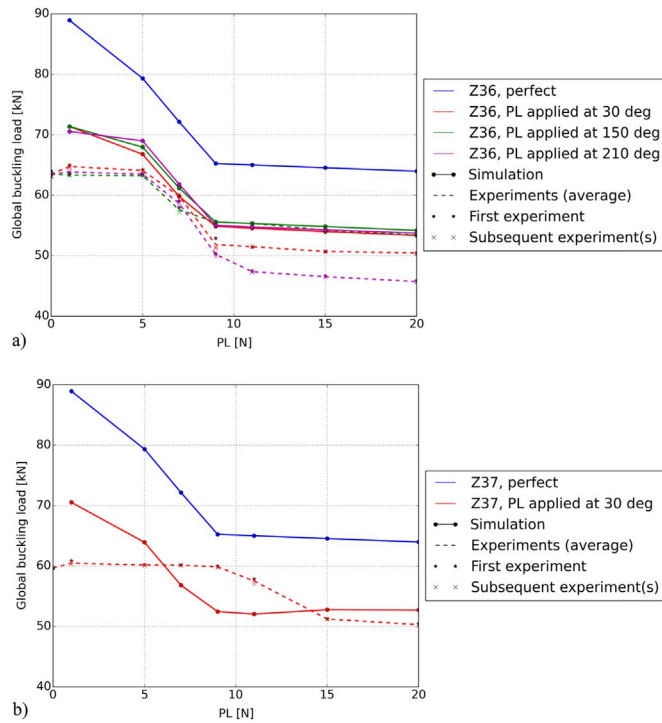
Fig. 17. Perturbation load curves for a) Z36 b) Z37.

Table 4
Comparison of KDF values for Z36 and Z37.

Structure	Z36	Z37
Linear buckling load (reference)	89.6 kN	89.6 kN
Knock-down factors		
NASA SP-8007	0.31 (27.8 kN)	0.31 (27.8 kN)
SPLA N1	0.73 (65.2 kN)	0.73 (65.2 kN)
FEA (MSI)	0.85 (76.4 kN)	0.87 (77 kN)
FEA (MSI + TI + FVF)	0.8 (71.3 kN)	0.79 (71.2 kN)
Test	0.71 (63.3 kN)	0.65 (58.3 kN)

take place at 0° and 120° in the middle of the shell, which is not reflected in the FEA, being a possible reason for the discrepancy between the test and FEA buckling loads.

The perturbation experimental and FEA load curves of Z37 are depicted in Fig. 17 (b). It can be seen that the difference between the buckling loads of tests and FEA with the small perturbation load values are quite high, whereas the difference between the FEA and test N1 values are negligible. Unlike Z36, the difference between the FEA and test P1 is quite significant.

6.2. Knock-down factors

Table 4 shows the linear buckling load values of the two test articles and the KDF values. The NASA SP-8007 delivers a KDF which is more than two times lower than the test KDF which is unnecessary too conservative.

The FEA KDFs of the imperfect FEA model differs for about 12.7% in the case of Z36 and for about 21% in the case of Z37 from the test results. As it was discussed in Section 4.2, slight imperfections in the load introduction into the shell were observed. Investigation on how the load introduction and boundary condition imperfection affect the buckling load is left for future studies.

In theory, the KDF values obtained by the SPLA are to be compared with the KDF values of simulations that include the MSI. This is due to the fact that the SPLA accounts for geometric imperfections only [5].

The KDF values obtained by SPLA are more conservative than the FEA (MSI) KDFs for both cylinders. The SPLA KDF values are, however, higher than the KDF values obtained in the tests, since in the experiments other influences such as irregularities in boundary condition and asymmetry in load introduction have an additional degrading effect that are not accounted by the approach.

7. Summary and conclusions

Buckling tests of two nominally identical composite laminated unstiffened cylinders under axial compression with and without lateral load were performed. The cylinders, denominated as Z36 and Z37, were examined before testing by means of ultrasonic testing and photogrammetry. Loads and axial displacements were recorded during tests and the results herein discussed. Additionally, the structural behavior of the test cylinders was monitored with strain gage readings and during selected buckling tests with the ARAMIS system. The NASA SP-8007 KDF, which comes to 0.31, is too conservative for the test results delivered. The measured geometric imperfections (mid-surface imperfections, thickness imperfections and fiber volume fraction correction) were included into the FE model. Including the measured imperfections reduces the difference between the test and FEA buckling load values. In the case of Z36 a relatively good agreement between the test and FEA results was reached. However, the FEA buckling load of the imperfect Z37 model deviated for more than 20% from the test load. The reason for this discrepancy is assumed to be caused by the load introduction and boundary condition imperfections. For the models' validation one needs to investigate the aforementioned effects which is left for future studies.

The SPLA is validated for Z36 and Z37 (R/t = 533.3 and H/R = 2, stacking sequence [34/−34/0/0/53/−53] by comparing the design buckling load N1 delivered by SPLA and the buckling load that includes the real measured geometric imperfections. However, the SPLA KDF value is not conservative enough when compared with the test buckling loads. That is because during experiments other influences such as boundary conditions and asymmetries in load introduction have a significant influence.

A new promising lower-bound method was proposed in [32] which considers the influence of geometric and load introduction imperfections on the buckling load. More experiments and studies correlating existing experiments are encouraged in order to validate novel approaches focused on the achievement of less conservative knock-down factors.

Acknowledgements

References

[1] W.T. Koiter, A translation of the stability of elastic equilibrium, Technische Hooge School at Delft, Department of Mechanics, Shipbuilding and Airplane Building. 14th November., 1945.
[2] V.I. Weingarten, P. Seide, J.P. Peterson, NASA SP-8007 - buckling of thin-walled circular cylinders, NASA Space Vehicle Design Criteria - Structures, 1965 (revised 1968).
[3] M. Nemeth, J. H. Starnes, The NASA Monographs on Shell Stability Design Recommendations, NASA/TP-1998-206290, Hampton, Virginia, 1998.

[4] M.W. Hilburger, Developing the next generation shell buckling design factors and technologies, in: Proceedings of the AIAA Preceedings, 2012.

[5] C. Hühne, R. Rolfes, E. Breitbach, J. Teßmer, Robust design of composite cylindrical shells under axial compression - simulation and validation, Thin-Walled Struct. 46 (2008) 947–962.

[6] M. Arbelo, R. Zimmermann, S. Castro, R. Degenhardt, Comparison of new design guidelines for composite cylindrical shells prone to buckling, 2013.

[7] J. Arbocz, J.H. Starnes Jr., Future directions and challenges in shell stability analysis, Thin-Walled Struct. 40 (2002) 729–754.

[8] M. W. Hilburger, M. P. Nemeth, J. H. Starnes Jr., Shell buckling design criteria based on manufacturing imperfection signatures, NASA Report TM-2004-212659, 2004.

[9] R. Degenhardt, A. Bethge, A. King, R. Zimmermann, K. Rohwer, J. Teßmer, A. Calvi, Probabilistic approach for improved buckling knock-down factors of CFRP cylindrical shells, in: Proceedings of the First CEAS European Air and Space Conference, 2008.

[10] R. Degenhardt, A. Kling, A. Bethge, J. Orf, L. Kärger, K. Rohwer, R. Zimmermann, A. Calvi, Investigations on imperfection sensitivity and deduction of improved knock-down factors for unstiffened CFRP cylindrical shells, Composite Struct. 92 (8) (2010) 1939–1946.

[11] M. Esslinger, Hochgeschwindigkeitsaufnahmen vom Beulvorgang dünnwandiger, axialbelasteter Zylinder, Der Stahlbau, vol. 3, 1970.

[12] M. Deml, W. Wunderlich, Direct evaluation of the "worst" imperfection shape in shell buckling, Comput. Methods Appl. Mech. Eng. 149 (1997) 201–222.

[13] M.A. Arbelo, R. Zimmermann, S.G.P. Castro, R. Degenhardt, Comparison of new design guidelines for composite cylindrical shells prone to buckling, in: Proceedings of the 9th International Conference on Composite Science and Technology, Sorrento, Naples, Italy, 2013.

[14] S.G.P. Castro, R. Zimmermann, M.A. Arbelo, R. Khakimova, M.W. Hilburger, R. Degenhardt, Geometric imperfections and lower-bound methods used to calculate knock-down factors for axially compressed composite cylindrical shells, Thin-Walled Struct. 74 (2014) 118–132.

[15] R. Khakimova, C.J. Warren, R. Zimmermann, S.G. Castro, M.A. Arbelo, R. Degenhardt, The single perturbation load approach applied to imperfection sensitive conical composite structures,", Thin-Walled Struct. 84 (2014) 369–377.

[16] R. Khakimova, R. Zimmermann, D. Wilckens, K. Rohwer, R. Degenhardt, Buckling of axially compressed CFRP truncated cones with additional lateral load: experimental and numerical investigation, Composite Struct. 157 (2016) 436–447.

[17] W.T. Haynie, M.W. Hilburger, Comparison of methods to predict lower bound buckling loads of cylinders under axial compression, in: Proceedings of the 51st AIAA/ASME/ASCE/AHS/ASC, 12-15 Apr., Orlando, FL, United States, 2010.

[18] M.A. Arbelo, R. Degenhardt, S.G.P. Castro, R. Zimmermann, Numerical characterization of imperfection sensitive composite structures, Composite Struct. 108 (2014) 295–303.

[19] R. Wagner, C. Hühne, Single perturbation load approach (SPLA) to determine buckling loads of composite shells under axial compression, in: Proceedings of the European Conference on Spacecraft Structures, Materials & Environmental Testing, Braunschweig, Germany, 2014.

[20] H. Wagner, C. Hühne, K. Rohwer, S. Niemann, M. Wiedemann, Stimulating the realistic worst case buckling scenario of axially compressed cylindrical composite shells, Composite Struct. 160 (2017) 1095–1104.

[21] H. Wagner, C. Hühne, S. Niemann, Constant single-buckle imperfection principle to determine a lower bound for the buckling load of unstiffened composite cylinders under axial compression, Composite Struct. 139 (2016) 120–129.

[22] D. S. Abaqus, User's Manual, Abaqus Analysis User's Manual, 2011.

[23] The European Association of Aerospace Industries, DIN EN 6031 Fibre reinforced plastics - Test method; determination of in-plane shear properties (± 45˚ tensile test), 1996.

[24] The European Association of Aerospace Industries, DIN EN 2850 Unidirektionale Kohlenstoffaser-Duroplast Verbundwerkstoffe Druckversuch parallel zur Faserrichtung, 1997.

[25] European Association of Aerospace Manufacturers, DIN EN 2561 Kohlenstofffaserverstärkte Kunststoffe Unidirektionale Laminate Zugprüfung parallel zur Faserrichtung, European Committee for Standardization, 1995.

[26] European Association of Aerospace Manufacturers, DIN EN 2597 Carbon fibre reinforced plastics, unidirectional laminates - Tensile test perpendicular to the fibre direction, 1998.

[27] H. Schürmann, Konstruieren mit Faser-Kunststoff-Verbunden, Springer, 2007.

[28] S.G. Castro et al., DESICOS Abaqus plug-in, 2014–2017. [Online]. Available: 〈https://github.com/desicos/desicos/〉. (accessed Apr.2016).

[29] R. Khakimova, D. Wilckens, J. Reichardt, R. Zimmermann, R. Degenhardt, Buckling of axially compressed CFRP truncated cones: experimental and numerical investigation, Composite Struct. 146 (2016) 232–247.

[30] G.O.M., User manual, ARAMIS v6.3 and higher, Braunschweig, 2011.

[31] S. Castro, Semi-Analytical Tools for the Analysis of laminated Composite Cylindrical and Conical Imperfect Shells under Various Loading and Boundary Conditions, Dissertation, TU Clausthal, 2015.

[32] H. Wagner, Hühne, S. Niemann, R. Khakimova, Robust design criterion for axially loaded cylindrical shells - simulation and validation (http://dx.doi.org/), Thin-Walled Struct. (2017), http://dx.doi.org/10.1016/j.tws.2016.12.017 (http://dx.doi.org/).